Energy dissipation in microfluidic beam resonators: Effect of Poisson's ratio

John E. Sader,[1,*] Thomas P. Burg,[2,3] Jungchul Lee,[2,4] and Scott R. Manalis[2,5]
[1]*Department of Mathematics and Statistics, The University of Melbourne, Victoria 3010, Australia*
[2]*Department of Biological Engineering, Massachusetts Institute of Technology, Cambridge, Massachusetts 02139, USA*
[3]*Max Planck Institute for Biophysical Chemistry, D-37077 Goettingen, Germany*
[4]*Department of Mechanical Engineering, Sogang University, Seoul 121-742, Korea*
[5]*Department of Mechanical Engineering, Massachusetts Institute of Technology, Cambridge, Massachusetts 02139, USA*
(Received 11 April 2011; revised manuscript received 21 June 2011; published 5 August 2011)

Dissipation of mechanical energy underlies the sensitivity of many nanomechanical devices, with environmental effects often having a significant effect. One case of practical relevance is the interaction of elastic beam resonators with fluid, which is known to dramatically increase energy dissipation. Recently, we investigated energy dissipation in a different class of elastic beam resonator that embeds a microfluidic channel in its interior. In this paper, we examine the effect of the beam material Poisson ratio on these devices and discover that it can strongly affect energy dissipation—this is in direct contrast to conventional cantilever beams immersed in fluid. Increasing the Poisson ratio in these microfluidic devices is found to decrease energy dissipation, with the incompressible material limit providing minimum energy dissipation. Our paper establishes that, in this limit, placement of the fluid channel away from the beam neutral axis has negligible effect on energy dissipation in many cases of practical interest. The physical implications of these findings are discussed, and a detailed comparison with available experimental results is provided.

DOI: 10.1103/PhysRevE.84.026304 PACS number(s): 47.90.+a, 87.85.Qr, 81.07.−b, 85.85.+j

I. INTRODUCTION

Cantilever beam resonators are often used as sensors for a range of applications, including the ultrasensitive detection of mass [1,2], accelerometers where they form the principal component [3], and the atomic force microscope (AFM) [4]. Knowledge of their dynamic properties is vital to many of these applications and often dictates the sensitivity to which measurements can be performed [2]. Immersion in fluid is of particular importance and is known to strongly enhance energy dissipation [5,6], thus, reducing measurement sensitivity [1,2]. Therefore, the ability to control and to predict this behavior is critical to the design and use of cantilever devices in fluid.

The dynamic properties of cantilever devices immersed in fluid have been studied widely [5–15]. Miniaturization has been shown to strongly increase the effects of fluid viscosity and to enhance energy dissipation in these systems [6]. For cantilever devices typically found in microelectromechanical systems and AFM, the observed quality factors in air are several orders of magnitude lower than their values in vacuum, with the immersion in liquid lowering the quality factors by a further 2 orders of magnitude [5,6]. These dramatic effects are enhanced upon further miniaturization, leading to strongly overdamped systems in liquid [6]. These features present a significant impediment to technological development, since they limit the sensing applications of micro- and nanoscale cantilevers in liquid. This is particularly relevant to mass and environmental sensing in biological and colloidal systems, where the resonant frequency shift of the cantilever is often monitored [1,2,16].

Recently, a different class of cantilever device was developed that embeds a microfluidic channel in its interior while evacuating the region exterior to the device [17–19]—these are commonly called suspended microchannel resonators; see Fig. 1. Mass sensing in these devices is achieved by flowing material in solution through the interior of the microfluidic channels—both flow-through and adsorption measurements are possible [17]. Importantly, the quality factors exhibited are orders of magnitude larger than conventional cantilever devices in the presence of fluid. This dramatically enhances the sensitivity of microfluidic beam resonators to environmental changes, allowing for the ultrasensitive detection of mass in liquid [17–19]. Theoretically, the mechanisms leading to this observed reduction in energy dissipation have been analyzed, with predictions in good agreement with measurements [20–22]. Interestingly, energy dissipation is a nonmonotonic function of fluid viscosity, allowing for an enhancement in quality factor through a reduction in device size. This contrasts strongly with conventional cantilever devices immersed in fluid, which exhibit a monotonic decrease in the quality factor with increasing viscosity or, equivalently, a uniform reduction in size [6]. Microfluidic cantilever devices overcome this fundamental difficulty and, thus, present a highly favorable structure for liquid sensing at the micro- and nanoscales.

In this paper, we expand on our previous work and examine the effect of Poisson's ratio on energy dissipation in these microfluidic beam devices. It is found that a nonzero (positive) Poisson ratio can strongly reduce energy dissipation and, thus, can enhance measurement sensitivity, for example, frequency shift resolution due to mass loading. This directly contrasts with conventional cantilevers, whose energy dissipation is independent of Poisson's ratio. The mechanisms leading to these disparate effects are discussed, and a simple analytical formula is presented for the effects described. Specifically, the effective channel placement away from the beam neutral axis Z_{eff} is found to be well approximated by

$$Z_{\text{eff}} \approx (1 - 2\sigma)\, Z_{\text{off-axis}}, \tag{1}$$

in many cases of practical interest, where $Z_{\text{off-axis}}$ is the true channel position from the neutral axis (see Fig. 2) and σ

*jsader@unimelb.edu.au

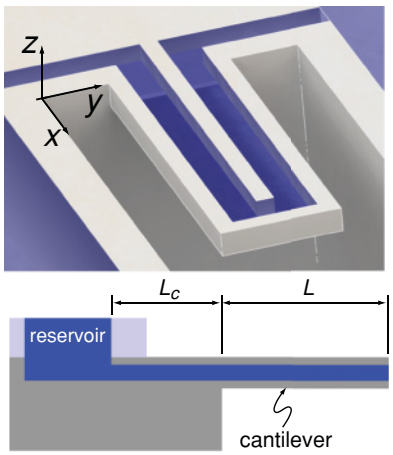

FIG. 1. (Color online) Illustration of the fluid channel embedded microcantilever. Perspective (top) layout of the embedded fluid channel, which is normally closed and here, shown open for illustration. Side view (bottom) cantilever structure (light gray—center of top, right side of bottom) showing cantilever length L and length of rigid lead channel L_c. Fluid channel (within cantilever) is completely filled with fluid—blue (dark gray).

is Poisson's ratio of the beam material. Flow generated by placement of the channel on the beam neutral axis is found to be unaffected by Poisson's ratio.

These findings open up a different dimension for tuning energy dissipation in microfluidic beam resonators, allowing for greater flexibility in design, manufacture, and application. Specifically, through the use of materials with Poisson's ratios near the incompressible limit ($\sigma = 1/2$), energy dissipation can strongly be reduced. From Eq. (1), it is evident that such devices are less sensitive to the effects of fluid channel placement away from the beam neutral axis, which is known

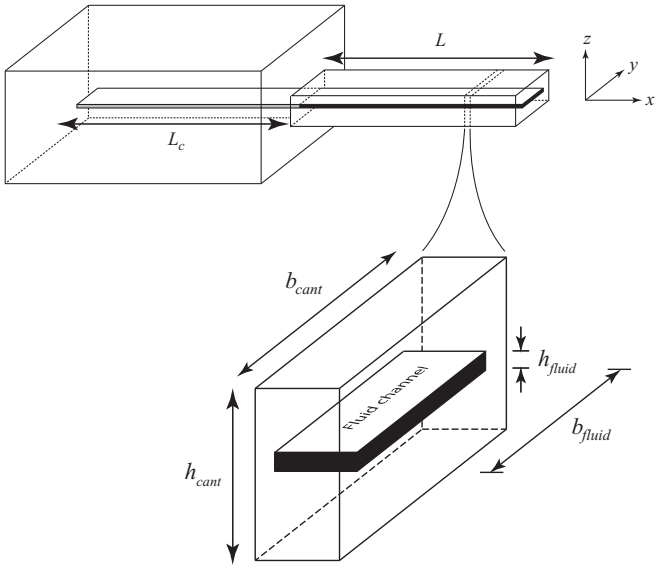

FIG. 2. Schematic of rectangular cantilever ($x > 0$) with the embedded fluid channel and rigid lead channel ($x < 0$) showing dimensions. The position of the fluid channel away from the neutral axis ($z = 0$) in the z direction is denoted as $Z_{\text{off-axis}} \equiv z_0$ The origin of the Cartesian coordinate system is the center of mass of the clamped end.

to strongly enhance energy dissipation [21]. The physical mechanisms leading to this finding will be discussed. Also, a comparison to available measurements over a range of fluids will be presented for the first two flexural modes of vibration.

We begin by summarizing the theoretical framework used in our previous paper, and we discuss the effect of Poisson's ratio on the beam deformation. This is followed by the complete solution to the fluid-structure interaction problem. The effects of placement of the channel both on and away from the neutral axis of the beam will be explored. Then, we present detailed numerical results examining the effect of Poisson's ratio on energy dissipation. The simple analytical formula in Eq. (1) is derived. Finally, a comparison of the derived theoretical model with experimental measurements will be presented, followed by practical recommendations. A first principles derivation of the displacement field of the Euler-Bernoulli beam theory [23] is presented in the Appendix due to its relevance to this paper.

II. THEORETICAL MODEL

In Refs. [20–22], we developed theoretical models for energy dissipation within the fluid channel of a microfluidic beam resonator. Here, we briefly review the underlying assumptions of these models since they also form the basis for the present model. Consider a rectangular cantilever beam with a thin embedded channel that contains fluid; see Fig. 2. The following geometric assumptions are imposed:

(A) The cantilever length L is much larger than its width b_{cant} and thickness h_{cant}.

(B) The fluid channel thickness h_{fluid} is much smaller than the channel width b_{fluid}; as a leading order approximation, we take the formal limit $h_{\text{fluid}}/b_{\text{fluid}} \to 0$ throughout. This enables the embedded fluid channel to be represented by a single channel whose total width is the sum of the two parallel channels widths, cf. Figs. 1 and 2.

(C) The fluid channel spans the entire length of the cantilever L, and the cantilever is vibrating in one of its flexural modes [22].

(D) The lead channel of length L_c within the substrate of the chip is rigid.

(E) The amplitude of oscillation is much smaller than any geometric length scale of the beam so that the convective inertial term in the Navier-Stokes equation can be ignored, and linear motion and flow are ensured [6].

Under these conditions [21], the displacement field in the solid is given by Euler-Bernoulli beam theory; see the Appendix for a detailed derivation of this classical theory, which also emphasizes its principal assumptions. This displacement field sets the boundary conditions that drive fluid motion within the channel.

A. Fluid boundary conditions

From Eq. (A8) of the Appendix, the displacement field of the beam material (for arbitrary Poisson's ratio σ) is given by

$$\mathbf{U}(x,y,z,t) = -z\frac{\partial W}{\partial x}\hat{\mathbf{x}} + \sigma yz\frac{\partial^2 W}{\partial x^2}\hat{\mathbf{y}} + \left[W(x,t) + \frac{\sigma}{2}(z^2 - y^2)\frac{\partial^2 W}{\partial x^2}\right]\hat{\mathbf{z}}, \quad (2)$$

where $W(x,t)$ is the beam deflection function, the Cartesian coordinate system is specified in Fig. 2, and t is time; W is zero inside the rigid lead channel ($x < 0$).

The model assumptions (A)–(C) indicate that terms dependent on the Poisson ratio in Eq. (2) are negligibly small [21]—they are $O(h_{\text{fluid}}/L)$ smaller than other terms and were omitted in the formulations of Refs. [20–22]. These Poisson ratio terms in Eq. (2) are indeed negligible for on-axis placement of the channel. However, their net effect on the fluid motion and energy dissipation can be of equal order to other terms when the fluid channel is placed away from the beam neutral axis, unless the Poisson ratio is zero. The physical reasons for these features and the situations where Poisson's ratio is important are discussed in detail below.

All dependent variables are expressed in terms of the explicit time dependence $e^{-i\omega t}$ such that

$$X(x,y,z,t) = \tilde{X}(x,y,z|\omega)e^{-i\omega t},$$

where ω is the radial frequency and i is the usual imaginary unit. Henceforth, for simplicity, we will omit the superfluous "$\sim$" notation, noting that the above relation holds universally. Consequently, the velocity field of the beam resulting from Eq. (2) is

$$\mathbf{V}(x,y,z|\omega) = -i\omega\left(-z\frac{dW}{dx}\hat{\mathbf{x}} + \sigma yz\frac{d^2W}{dx^2}\hat{\mathbf{y}} + \left[W(x) + \frac{\sigma}{2}(z^2 - y^2)\frac{d^2W}{dx^2}\right]\hat{\mathbf{z}}\right). \quad (3)$$

The beam deflection function W is found by solving the Euler-Bernoulli beam equation, subject to clamped-free boundary conditions

$$W(x) = A\frac{(-1)^n}{2}\left(\left[\cos\left(C_n\frac{x}{L}\right) - \cosh\left(C_n\frac{x}{L}\right)\right] + \frac{\cos C_n + \cosh C_n}{\sin C_n + \sinh C_n}\left[\sinh\left(C_n\frac{x}{L}\right) - \sin\left(C_n\frac{x}{L}\right)\right]\right), \quad (4a)$$

where A is the oscillation amplitude at the free end of the cantilever ($x = L$), $n = 1,2,3,\ldots$ is the mode number, and C_n is the nth positive root of

$$\cosh C_n \cos C_n = -1. \quad (4b)$$

Fluid flow in the channel is driven by the solid velocity as specified in Eq. (3).

Note that terms in Eq. (3), dependent on Poisson's ratio, produce a distortion of the beam cross section [24] as the beam deflects. This distortion is illustrated in Fig. 3 for a range of Poisson's ratios and is in addition to the extension in the x direction and vertical deflection in the z direction; the latter deformations are both independent of Poisson's ratio; see Eq. (3). The net effect of this cross-sectional distortion on the flow generated in the fluid channel is now investigated.

The center of the fluid channel is positioned at $z = z_0$, and thus, is z_0 away from the neutral axis of the beam. From Eq. (3), velocities of the upper and lower surfaces of the channel are

$$\mathbf{V}\left(x,y,z_0 \pm \frac{h_{\text{fluid}}}{2}\,\middle|\,\omega\right) = -i\omega\left(-\left(z_0 \pm \frac{h_{\text{fluid}}}{2}\right)\frac{dW}{dx}\hat{\mathbf{x}} + \sigma y\left(z_0 \pm \frac{h_{\text{fluid}}}{2}\right)\frac{d^2W}{dx^2}\hat{\mathbf{y}} + \left\{W(x|\omega) + \frac{\sigma}{2}\left[\left(z_0 \pm \frac{h_{\text{fluid}}}{2}\right)^2 - y^2\right]\frac{d^2W}{dx^2}\right\}\hat{\mathbf{z}}\right), \quad (5)$$

where h_{fluid} is the channel thickness. By expanding Eq. (5) and collecting terms of equal power in the off-axis placement, z_0 then gives

$$\mathbf{V}\left(x,y,\, z_0 \pm \frac{h_{\text{fluid}}}{2}\,\middle|\,\omega\right) = -i\omega\sum_{m=0}^{2} z_0^m \mathbf{F}_m(x,y|\omega), \quad (6)$$

where

$$\mathbf{F}_0(x,y|\omega) = z_d\left[-\frac{dW}{dx}\hat{\mathbf{x}} + \sigma y\frac{d^2W}{dx^2}\hat{\mathbf{y}}\right] + \left[W(x|\omega) + \frac{\sigma}{2}\left(z_d^2 - y^2\right)\frac{d^2W}{dx^2}\right]\hat{\mathbf{z}}, \quad (7a)$$

$$\mathbf{F}_1(x,y|\omega) = -\frac{dW}{dx}\hat{\mathbf{x}} + \sigma y\frac{d^2W}{dx^2}\hat{\mathbf{y}} + \sigma z_d\frac{d^2W}{dx^2}\hat{\mathbf{z}}, \quad (7b)$$

$$\mathbf{F}_2(x,y|\omega) = \frac{\sigma}{2}\frac{d^2W}{dx^2}\hat{\mathbf{z}}, \quad (7c)$$

where $z_d = z - z_0 = \pm h_{\text{fluid}}/2$ at the upper and lower surfaces of the channel. Since the fluid channel is assumed to be infinitely thin ($h_{\text{fluid}}/b_{\text{fluid}} \to 0$), in accord with Assumption (B), the velocity boundary conditions at the edges of the channel are specified implicitly in Eq. (7).

From Eq. (6), it is evident that $\mathbf{F}_0(x,y|\omega)$ specifies flow boundary conditions for the placement of the channel on the beam neutral axis, i.e., $z_0 = 0$. The terms $\mathbf{F}_1(x,y|\omega)$ and $\mathbf{F}_2(x,y|\omega)$ yield corrections due to the placement of the

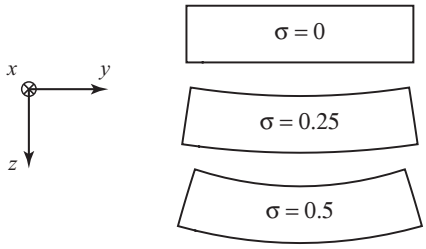

FIG. 3. Deformation of the beam cross section, as a function of Poisson's ratio, illustrating distortion with increasing Poisson's ratio: $\sigma = 0,\ 0.25,\ 0.5$. Cartesian coordinate system indicated.

channel away from the neutral axis. Since the problem is linear, flows generated by these three terms can be solved independently and later can be combined to obtain the complete solution. We now examine the individual components within these three terms and assess their relative contributions in the limit of an infinitely thin channel, i.e., $h_{\text{fluid}}/L \to 0$.

1. On-axis placement

We begin with the placement of the fluid channel on the beam neutral axis, i.e., $z_0 = 0$. Since no axial force is applied, the beam is inextensible, and the net extension and compression of the fluid channel is zero, as discussed in the Appendix. As such, the volumetric flux along the channel is zero, and $\mathbf{F}_0(x,y\,|\omega)$ generates a localized shear flow at any point (x_0,y_0). Thus, we expand $\mathbf{F}_0(x,y\,|\omega)$ about the planar position (x_0,y_0) to determine its local contribution,

$$\mathbf{F}_0(x,y|\omega) = W(x_0|\omega)\,\hat{\mathbf{z}} + [-z\,\hat{\mathbf{x}} + (x-x_0)\,\hat{\mathbf{z}}]\left.\frac{dW}{dx}\right|_{(x_0,y_0)} + \cdots, \tag{8}$$

where $z = \pm h_{\text{fluid}}/2$ at the upper and lower surfaces of the channel. The length scale over which the deflection function W varies is the beam length L. However, since the flow is localized at (x_0,y_0), the hydrodynamic length scale for all other Cartesian coordinates is the fluid channel thickness h_{fluid}. Furthermore, an underlying assumption in Euler-Bernoulli beam theory is that the cantilever length greatly exceeds its width and thickness; see the Appendix. It then follows that all terms neglected in Eq. (8) are of higher order and, hence, are negligible in this formal limit $h_{\text{fluid}}/L \to 0$, $b_{\text{fluid}}/L \to 0$ [21].

Since Eq. (8) is independent of Poisson's ratio, this analysis establishes that Poisson's ratio has no effect on the on-axis flow. Consequently, the models in Refs. [20–22] for on-axis flow are formally valid for all Poisson's ratios.

2. Off-axis placement

Next, the additional flow generated by the placement of the fluid channel away from the neutral axis is considered, i.e., $z_0 \neq 0$.

This flow results from the boundary conditions specified by $\mathbf{F}_1(x,y|\omega)$ and $\mathbf{F}_2(x,y|\omega)$ in Eq. (7). In the limit of zero Poisson's ratio, $\mathbf{F}_2(x,y|\omega)$ vanishes while $\mathbf{F}_1(x,y|\omega)$ has a component in the x direction only. This latter component was analyzed in the formulation of Ref. [21]. We now examine the contributions of $\mathbf{F}_1(x,y|\omega)$ and $\mathbf{F}_2(x,y|\omega)$ for nonzero Poisson's ratio.

Function $\mathbf{F}_1$. We begin with the boundary condition specified by $\mathbf{F}_1(x,y|\omega)$. The displacement field of the beam corresponding to $\mathbf{F}_1(x,y|\omega)$ is

$$\mathbf{U}_1(x,y,z|\omega) = z_0\left[-\frac{dW}{dx}\hat{\mathbf{x}} + \sigma y\frac{d^2W}{dx^2}\hat{\mathbf{y}} + \sigma\,(z-z_0)\frac{d^2W}{dx^2}\hat{\mathbf{z}}\right], \tag{9}$$

whose divergence is

$$\boldsymbol{\nabla}\cdot\mathbf{U}_1 = -\,z_0(1-2\sigma)\frac{d^2W}{dx^2}. \tag{10}$$

Equation (10) establishes that the volume change in the channel generated by this boundary condition depends on Poisson's ratio—an incompressible solid ($\sigma = 1/2$) yields no net volume change in the channel. As the beam extends in the x direction, it contracts in the y and z directions in accord with Poisson's ratio of the material; see Eq. (9). Consequently, the off-axis pumping mechanism described in Ref. [21] can strongly be modified by Poisson's ratio σ.

Function $\mathbf{F}_2$. Importantly, $\mathbf{F}_2(x,y|\omega)$ does not yield a change in channel volume since its divergence is zero—it produces a shear flow parallel to the z direction. This is similar to $\mathbf{F}_0(x,y|\omega)$ and results in localized flow at any planar position (x_0,y_0). Comparing $\mathbf{F}_0(x,y|\omega)$ and $\mathbf{F}_2(x,y|\omega)$ immediately establishes that $\mathbf{F}_2(x,y|\omega)$ is of similar order to the (negligible) higher order terms of $\mathbf{F}_0(x,y|\omega)$ in Eq. (8). Consequently, $\mathbf{F}_2(x,y|\omega)$ also produces a negligible contribution.

To summarize, we find that, under the assumptions of Euler-Bernoulli beam theory, (i) the *on-axis flow* is independent of Poisson's ratio, whereas, (ii) the *off-axis flow* is generated solely by $\mathbf{F}_1(x,y|\omega)$ and depends strongly on Poisson's ratio. Therefore, the flow generated by the on-axis problem is identical to that given in Ref. [21].

We examine the flow induced by $\mathbf{F}_1(x,y|\omega)$ for an arbitrary Poisson ratio in the next section.

B. Off-axis flow for an arbitrary Poisson ratio

Analysis of the off-axis flow for an arbitrary Poisson ratio follows along similar lines to that given in Ref. [21]. Therefore, we only present the essential details and refer the reader to Ref. [21] for a more comprehensive discussion; identical notation and functions to those of Ref. [21] will be used where possible.

Since the flow is not localized, we consider the entire rigid lead channel and cantilever system. The length of the rigid lead channel is defined to be L_c, and the origin of the coordinate system is at the clamped end of the cantilever; see Fig. 2.

Because high pressures can be generated [21] in the fluid channel, we consider the case of viscous compressible flow. The governing equations in the time domain are the linearized compressible Navier-Stokes equations [see Assumption (E)],

$$\begin{aligned}\frac{\partial\rho}{\partial t} + \rho\boldsymbol{\nabla}\cdot\boldsymbol{v} &= 0,\\ \rho\frac{\partial\boldsymbol{v}}{\partial t} &= -\boldsymbol{\nabla}P + \mu\,\nabla^2\boldsymbol{v} + \frac{1}{3}\mu\boldsymbol{\nabla}(\boldsymbol{\nabla}\cdot\boldsymbol{v}),\end{aligned} \tag{11}$$

where $\boldsymbol{v}$ is the velocity field of the fluid, P is the pressure, and μ is fluid shear viscosity. The Stokes hypothesis has been invoked in Eq. (11), i.e., the bulk viscosity μ_B is set to zero, but this is of no consequence to the final solution as discussed in Ref. [21]. In this (linear) limit of small amplitude, the corresponding equation of state for the fluid is as follows:

$$\rho = \rho_0 + \rho_0\kappa P, \tag{12}$$

where κ is the compressibility of the fluid and is related to the speed of sound c by $\kappa = 1/(\rho_0 c^2)$ and ρ_0 is the fluid density at

ambient pressure ($P = 0$). Substituting Eq. (12) into Eq. (11) and noting the time ansatz used previously then gives

$$\begin{aligned} \nabla \cdot \boldsymbol{v} &= i\omega\kappa P, \\ -i\omega\rho_0 \boldsymbol{v} &= -\left(1 - \tfrac{1}{3} i\mu\omega\kappa\right)\nabla P + \mu\nabla^2 \boldsymbol{v}. \end{aligned} \tag{13}$$

For clarity of exposition, the displacement and velocity fields of the fluid are denoted by lowercase symbols, whereas, those of the solid (beam) are denoted by capitals.

Since the cantilever length L greatly exceeds the channel thickness h_{fluid}, we scale the x coordinate by L, the y coordinate by b_{fluid}, and the z coordinate by h_{fluid}. The pressure scale is also chosen to be appropriate for the low inertia limit, and the velocity scales are obtained from the boundary conditions and continuity equation. This leads to the following set of scales:

$$\begin{aligned} x_s = L, \quad y_s = b_{\text{fluid}}, \quad z_s = h_{\text{fluid}}, \quad u_s = i\omega z_0 \left.\frac{dW}{dx}\right|_{x=L}, \\ v_s = \frac{b_{\text{fluid}}}{L} u_s, \quad w_s = \frac{h_{\text{fluid}}}{L} u_s, \quad P_s = \frac{\mu u_s L}{h_{\text{fluid}}^2}, \end{aligned} \tag{14}$$

where the subscript s indicates a scaling. Substituting Eq. (14) into Eq. (13) and noting that $L \gg b_{\text{fluid}} \gg h_{\text{fluid}}$ then gives the required leading order scaled governing equations,

$$\frac{\partial \bar{u}}{\partial \bar{x}} + \frac{\partial \bar{v}}{\partial \bar{y}} + \frac{\partial \bar{w}}{\partial \bar{z}} = i\alpha \bar{P}, \quad -i\beta\, \bar{u} = -\frac{d\bar{P}}{d\bar{x}} + \frac{\partial^2 \bar{u}}{\partial \bar{z}^2}, \tag{15}$$

where an overscore indicates a scaled variable, the velocity field is $\boldsymbol{v} = u\hat{\mathbf{x}} + v\hat{\mathbf{z}} + w\hat{\mathbf{z}}$, the pressure is independent of y and z, to leading order, and the following dimensionless variables naturally arise:

$$\beta = \frac{\rho_0 \omega h_{\text{fluid}}^2}{\mu}, \quad \gamma = \left(\frac{\omega L}{c}\right)^2, \quad \alpha = \frac{\gamma}{\beta}, \tag{16}$$

These variables have the following physical interpretations:

(i) β is the squared ratio of the channel thickness to the viscous penetration depth and indicates the importance of *fluid inertia*. This parameter is commonly referred to as the *Reynolds number* [25,26].

(ii) γ is the squared ratio of the cantilever length to the acoustic wavelength and indicates the importance of acoustic effects. This is termed the *normalized wave number*.

(iii) α is the ratio of γ and β and dictates when fluid compressibility significantly affects the flow due to *variations in fluid density* via the pressure. It is termed the *fluid compressibility number*.

Equation (15) is correct to leading order for small h_{fluid}/L and b_{fluid}/L, while Euler-Bernoulli beam theory is also derived in the asymptotic limit of small h/L and b/L. Thus, the governing equations for the solid and fluid are formally consistent asymptotic theories; see Sec. 3.5 of Ref. [21] for further discussion.

In Ref. [21], the free end of the beam ($\bar{x} = 1$) was chosen as the origin of the (moving) reference frame in which the problem was solved. This change of frame inherently accounted for the volume variations in the channel, since the reduced problem (for zero Poisson's ratio) corresponded to a channel whose sidewalls were straining purely in their plane in an infinite fluid reservoir. For nonzero Poisson's ratio, however, the channel walls deform in all three dimensions, see Eq. (17), and this change of frame provides no such conceptual advantage. Thus, in contrast to Ref. [21], we solve the problem in the original (fixed) reference frame of the beam. The scaled boundary conditions at the channel walls follow from Eqs. (6), (7b), and (14) and the use of the usual no-slip condition,

$$(\bar{u}, \bar{v}, \bar{w})|_{\bar{z}=\bar{z}_0 \pm \frac{1}{2}} = \begin{cases} (1 + S(\bar{x}), -\sigma \bar{y} S'(\bar{x}), \mp \frac{\sigma}{2} S'(\bar{x})), & 0 \leqslant \bar{x} \leqslant 1 \\ 0, & -\bar{L}_c \leqslant \bar{x} < 0 \end{cases} \tag{17}$$

where

$$S(\bar{x}) = \frac{\frac{dW}{d\bar{x}} - \left.\frac{dW}{d\bar{x}}\right|_{\bar{x}=1}}{\left.\frac{dW}{d\bar{x}}\right|_{\bar{x}=1}}. \tag{18}$$

Motivated by the boundary conditions in Eq. (17), we then search for a solution of the form

$$\begin{aligned} \bar{u} = f(\bar{x})k'(\bar{z}) + 2\sigma S(\bar{x}) + h(\bar{x}) + 1, \quad \bar{v} = -\sigma \bar{y} S'(\bar{x}), \\ \bar{w} = -f'(\bar{x})\, k(\bar{z}) - \sigma\, \bar{z}\, S'(\bar{x}), \end{aligned} \tag{19}$$

where the functions $f(\bar{x})$, $h(\bar{x})$, and $k(\bar{x})$ are to be determined. Substituting Eq. (19) into Eqs. (15) and (17) then gives

$$\frac{dh}{d\bar{x}} = i\alpha \bar{P}, \tag{20a}$$

$$\frac{d\bar{P}}{d\bar{x}} = Bf(\bar{x}) + i\beta[2\sigma S(\bar{x}) + h(\bar{x}) + 1], \tag{20b}$$

$$k'''(\bar{z}) + i\beta k'(\bar{z}) = B \tag{20c}$$

$$k\left(\pm\frac{1}{2}\right) = 0, \quad k'\left(\pm\frac{1}{2}\right) = 1, \tag{20d}$$

$$f(\bar{x}) = (1 - 2\sigma)S(\bar{x}) - h(\bar{x}), \tag{20e}$$

where B is a constant. Solving Eqs. (20c) and (20d) yields the solution for k,

$$k(\bar{z}) = \frac{\sinh\left((1-i)\sqrt{\frac{\beta}{2}}\,\bar{z}\right) - 2\bar{z}\sinh\left(\frac{1-i}{2}\sqrt{\frac{\beta}{2}}\right)}{(1-i)\sqrt{\frac{\beta}{2}}\cosh\left(\frac{1-i}{2}\sqrt{\frac{\beta}{2}}\right) - 2\sinh\left(\frac{1-i}{2}\sqrt{\frac{\beta}{2}}\right)}, \tag{21a}$$

and the constant B,

$$B = \frac{-2i\beta\sinh\left(\frac{1-i}{2}\sqrt{\frac{\beta}{2}}\right)}{(1-i)\sqrt{\frac{\beta}{2}}\cosh\left(\frac{1-i}{2}\sqrt{\frac{\beta}{2}}\right) - 2\sinh\left(\frac{1-i}{2}\sqrt{\frac{\beta}{2}}\right)}, \tag{21b}$$

where

$$\bar{z} = \frac{z - z_0}{h_{\text{fluid}}}. \tag{22}$$

Substituting Eq. (20e) into Eq. (19) then gives the required velocity field,

$$\begin{aligned} \bar{u} &= [(1-2\sigma)S(\bar{x}) - h(\bar{x})]k'(\bar{z}) + 2\sigma S(\bar{x}) + h(\bar{x}) + 1, \\ \bar{v} &= -\sigma \bar{y} S'(\bar{x}), \\ \bar{w} &= -[(1-2\sigma)S'(\bar{x}) - h'(\bar{x})]k(\bar{z}) - \sigma \bar{z} S'(\bar{x}), \end{aligned} \tag{23}$$

where the governing equation for $h(\bar{x})$ is obtained from Eqs. (20a) and (20b),

$$\begin{aligned} &\frac{d^2h}{d\bar{x}^2} + \alpha(\beta + iB)h \\ &\quad = \alpha(1-2\sigma)(\beta + iB)S(\bar{x}) - \alpha\beta[1 + S(\bar{x})] \end{aligned} \tag{24}$$

The function $h(\bar{x})$ is termed the *associated pressure function* due to its connection to the pressure distribution via Eq. (20a). The boundary conditions for $h(\bar{x})$ are obtained by (i) ensuring the pressure at the inlet to the channel ($\bar{x} = -\bar{L}_c$) equals the ambient pressure in the reservoir [21] and (ii) the x component of the velocity matches Eq. (17) at the free end of the cantilever ($\bar{x} = 1$)

$$h'(-\bar{L}_c) = h(1) = 0. \tag{25}$$

The solution to Eqs. (24) and (25) is easily evaluated using the Green's function method

$$\begin{aligned} h(\bar{x}) = &-\frac{\alpha}{M\cos[M(1+\bar{L}_c)]} \\ &\times \left\{ \sin[M(1-\bar{x})] \int_{-\bar{L}_c}^{\bar{x}} g(x')\cos[M(x'+\bar{L}_c)]\,dx' \right. \\ &\left. + \cos[M(\bar{x}+\bar{L}_c)] \int_{\bar{x}}^{1} g(x')\sin[M(1-x')]\,dx' \right\} \end{aligned} \tag{26}$$

where

$$g(\bar{x}) = (1-2\sigma)(\beta + iB)S(\bar{x}) - \beta[1 + S(\bar{x})] \tag{27a}$$

$$M = \sqrt{\alpha(\beta + iB)}, \tag{27b}$$

and the scaled pressure is obtained from Eq. (20a),

$$\bar{P} = \frac{1}{i\alpha}\frac{dh}{d\bar{x}}. \tag{28}$$

The rate-of-strain tensor for this velocity field is

$$\begin{aligned} \mathbf{e} = &\frac{i\omega z_0}{2h_{\text{fluid}}} \left.\frac{dW}{dx}\right|_{x=L} [(1-2\sigma)S(\bar{x}) - h(\bar{x})]\, k''(\bar{z}) \\ &\times (\hat{\mathbf{x}}\hat{\mathbf{z}} + \hat{\mathbf{z}}\hat{\mathbf{x}}) + O\left(\frac{h_{\text{fluid}}}{L}\right). \end{aligned} \tag{29}$$

C. Quality factor

We now present expressions for the quality factor of the device. Since the above analysis is derived at an arbitrary radial frequency of oscillation ω, it is applicable to any mode of vibration. This is of course provided that the underlying assumptions of the Euler-Bernoulli beam theory and the corresponding fluid-structure interaction problem are satisfied [22].

The quality factor is defined by

$$Q = 2\pi \left.\frac{E_{\text{stored}}}{E_{\text{diss/cycle}}}\right|_{\omega = \omega_R}, \tag{30}$$

where E_{stored} is the maximum energy stored in the mode, $E_{\text{diss/cycle}}$ is the energy dissipated per cycle in that mode, and ω_R is the radial resonant frequency of the mode. The energy dissipated per cycle $E_{\text{diss/cycle}}$ is easily calculated using Eq. (8) of Ref. [21], whereas, the maximum energy stored is obtained from the usual Euler-Bernoulli beam theory formula [23,24].

Using the on-axis result in Ref. [21] and the formulas derived above for the off-axis flow then yields the required result for an arbitrary Poisson ratio,

$$Q = F(\beta)\frac{\rho_{\text{cant}}}{\rho}\left(\frac{h_{\text{cant}}}{h_{\text{fluid}}}\right)\left(\frac{b_{\text{cant}}}{b_{\text{fluid}}}\right)\left(\frac{L}{h_{\text{fluid}}}\right)^2, \tag{31}$$

where the normalized quality factor is given by

$$F(\beta) = \frac{\beta}{16\int_{-\bar{L}_c}^{1}\int_{-1/2}^{1/2} |G(X,Z)|^2\, dZ\, dX}, \tag{32}$$

and

$$\begin{aligned} &G(X,Z) \\ &= \left(1 - \frac{1-i}{2}\sqrt{\frac{\beta}{2}}\frac{\cosh\left[(1-i)\sqrt{\frac{\beta}{2}}\,Z\right]}{\sinh\left(\frac{1-i}{2}\sqrt{\frac{\beta}{2}}\right)}\right)\frac{d\bar{W}}{dX} \\ &\quad + \frac{i\beta\bar{Z}_0}{2}\left(\frac{\sinh\left[(1-i)\sqrt{\frac{\beta}{2}}\,Z\right]}{(1-i)\sqrt{\frac{\beta}{2}}\cosh\left(\frac{1-i}{2}\sqrt{\frac{\beta}{2}}\right) - 2\sinh\left(\frac{1-i}{2}\sqrt{\frac{\beta}{2}}\right)}\right) \\ &\quad \times [(1-2\sigma)S(X) - h(X)]\left.\frac{d\bar{W}}{dX}\right|_{X=1}, \end{aligned} \tag{33a}$$

$$X = \frac{x}{L}, \quad Z = \frac{z - z_0}{h_{\text{fluid}}}, \quad \bar{Z}_0 = \frac{z_0}{h_{\text{fluid}}}, \quad \bar{L}_c = \frac{L_c}{L}, \tag{33b}$$

where $\bar{W}(X)$ is the normalized deflection function of the mode under consideration such that $\bar{W}(1) = 1$. The other required functions $S(X)$ and $h(X)$ are defined in Eqs. (18) and (26), respectively.

We denote the normalized deflection function of the nth mode of vibration $\bar{W}(X) = \bar{W}_n(X)$, whose solution is obtained directly from Eqs. (4), i.e.,

$$\begin{aligned} \bar{W}_n(X) = \frac{(-1)^n}{2}\Big[&(\cos C_n X - \cosh C_n X) \\ &+ \frac{\cos C_n + \cosh C_n}{\sin C_n + \sinh C_n}(\sinh C_n X - \sin C_n X)\Big], \end{aligned} \tag{34a}$$

where C_n is the nth positive root of

$$\cosh C_n \cos C_n = -1. \tag{34b}$$

All dimensionless variables β, γ, and α are evaluated at the resonant frequency $\omega = \omega_R$ of the mode of vibration under consideration; see Eq. (16).

III. RESULTS AND DISCUSSION

We now investigate the effect of Poisson's ratio using this theoretical model. The discussion will focus on the off-axis problem, since the on-axis flow is independent of Poisson's ratio and was considered in detail in Ref. [21]. We also consider the practically relevant case of $0 \leqslant \sigma \leqslant 1/2$ [24]. First, analytical forms of the equations are assessed, following which, a detailed comparison to numerical results will be presented. We will conclude with a quantitative comparison to experimental measurements and practical recommendations.

A. Incompressible flow

To begin, the limiting case of incompressible flow is considered, for which the fluid compressibility number is $\alpha = 0$. Since $h(X)$ is directly proportional to α, it follows from Eq. (26) that $h(X) = 0$ for incompressible flow; $h(X)$ contains all fluid compressibility effects. Equation (33a) then establishes that rescaling of the zero Poisson ratio solution [21] by

$$\bar{Z}_0 \to (1 - 2\sigma)\, \bar{Z}_0, \tag{35}$$

exactly accounts for the effect of the nonzero Poisson ratio. The underlying physical reason for this behavior is that the volumetric flux induced by pumping in the off-axis flow is directly proportional to $(1 - 2\sigma)\, \bar{Z}_0$; see Eq. (10). Thus, increasing Poisson's ratio from zero leads to a reduction in the effects of this pumping mechanism and, hence, less sensitivity to off-axis placement $\bar{Z}_0$ of the channel. In the limit of an incompressible solid ($\sigma = 1/2$), the volumetric flux into the channel is zero, and the energy dissipation vanishes for all $\bar{Z}_0$.

B. Compressible flow

With this result in hand, the general case of compressible flow is considered, i.e., $\alpha > 0$. It was shown in Refs. [20–22] that the effects of fluid compressibility on the off-axis flow are paramount for practical devices and cannot be ignored. Unlike the incompressible flow limit, Eqs. (26) and (27a) establish that the rescaling $(1 - 2\sigma)\, \bar{Z}_0$ is not exact for compressible flow. However, provided the first term dominates the second one in Eq. (27a), i.e., if $|B| \gg \beta$ and/or the function $h(X)$ is small, the rescaling in Eq. (35) will hold approximately. Note that, in the singular limit of an incompressible solid, i.e., $\sigma = 1/2$, the second term in Eq. (27a) will dominate the first always, thus rendering the condition $|B| \gg \beta$ irrelevant. The consequences of this property for an incompressible solid will be examined further below.

From Fig. 4, we find that the inequality $|B| \gg \beta$ is satisfied only in the low fluid inertia regime, i.e., $\beta \ll 10$. However, contribution of the on-axis flow to the total energy dissipation dominates that of the off-axis flow in the (complementary) high fluid inertia regime. Thus, violation of the condition $|B| \gg \beta$ is of little practical consequence to the total energy dissipation in the high fluid inertia regime. Therefore, the rescaling in Eq. (35) can be used to predict the effect of Poisson's ratio on the total energy dissipation in the device, regardless of fluid inertia for many cases of practical interest—exceptions do exist, which we will now discuss.

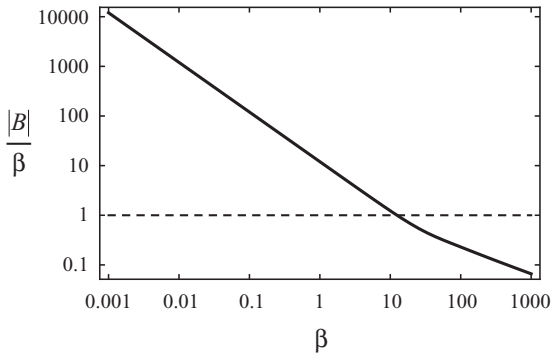

FIG. 4. Plot of $|B|/\beta$ vs β, defined in Eq. (21b). Horizontal line at unity is presented as a guide only.

We focus on the limit of high fluid inertia ($\beta \gg 10$) where the inequality $|B| \gg \beta$ no longer holds. In this limit, the governing equation in Eq. (24), for the function $h(X)$, which contains all fluid compressibility effects, becomes

$$\frac{d^2h}{dX^2} + \gamma h = -\gamma\,[1 + 2\sigma S(X)], \tag{36}$$

with $h'(-\bar{L}_c) = h(1) = 0$. Equation (36) establishes that, if the acoustic wavelength is large in comparison to the cantilever length, i.e., $\gamma \ll 1$, the function $h(X)$ is negligibly small. In this case, Eq. (33a) then indicates that the dependence on off-axis channel placement of the energy dissipation is well approximated by the Poisson ratio rescaling in Eq. (35) at high fluid inertia—this is expected, since the flow is approximately incompressible with (acoustic) wave motion being suppressed. However, in the small acoustic wavelength limit $\gamma \gg 1$, the right hand side of Eq. (36) exerts a significant effect, and the rescaling in Eq. (35) no longer holds. Here, acoustic effects are significant, and the flow can strongly deviate from the incompressible flow limit. We emphasize that this feature is not of major practical significance because the off-axis flow dominates the energy dissipation primarily in the low inertia regime as discussed above.

Nonetheless, situations do exist where fluid compressibility effects dominate at high fluid inertia ($\beta \gg 10$), but these rarely occur in practice and require generation of acoustic resonances by the off-axis flow [21]. In such cases, the rescaling in Eq. (35) is not applicable. Even so, these singular cases are difficult to realize experimentally [22], and thus, Eq. (35) can be used in the preliminary design and characterization of device behavior. Most importantly, Eq. (35) establishes that the use of a high Poisson ratio material reduces the effect of off-axis channel placement in many cases of practical interest.

These findings along with the regime of validity of Eq. (35) will be investigated numerically in the next section.

C. Numerical results

Numerical results illustrating the effects of Poisson's ratio on the flow behavior and energy dissipation (quality factor) are now presented. Results will be given for the fundamental mode in this numerical study, with the effects of higher order modes considered in the comparison to experimental measurements in Sec. III D. Throughout this section, we consider the typical practical case where the length of the rigid lead channel equals

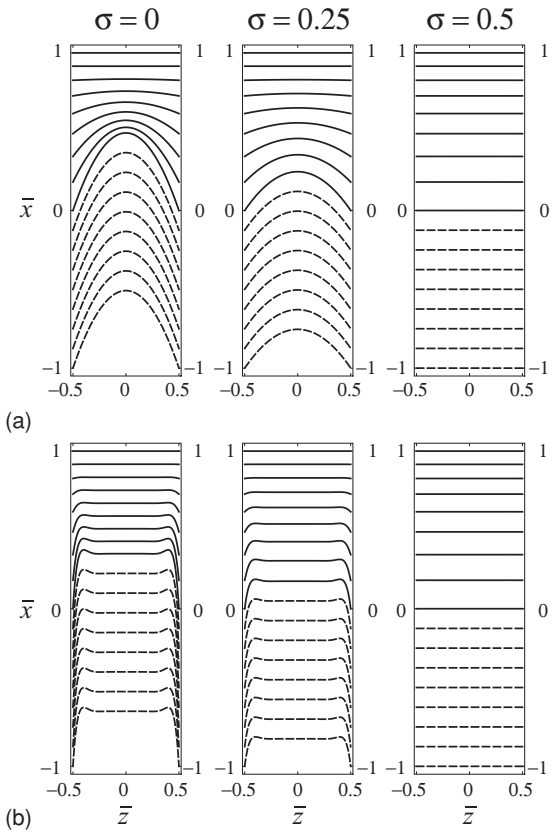

FIG. 5. Velocity profile (magnitude) within the rigid channel-cantilever system showing effects of Poisson's ratio $\sigma = 0,\ 0.25,\ 0.5$ for the *very low acoustic wave number* $\gamma = 0.001$. Velocity is scaled differently in rigid lead channel and cantilever for presentation only. Variation in fluid velocity relative to wall velocity for $\bar{x} \in [-1,1]$ and $\Delta\bar{x} = 0.125$. Different distance scalings used for the cantilever and rigid channel for clarity. Note. $\bar{x} = 0$ corresponds to the clamped end of the cantilever. (a) Low fluid inertia, $\beta = 0.1$, (b) high fluid inertia, $\beta = 1000$.

the cantilever length, i.e., $L_c = L$. All equations presented in Sec. II were implemented numerically using MATHEMATICA8.0.

1. Velocity field

To begin, we examine the effect of Poisson's ratio on the velocity field due to the off-axis flow only; the on-axis flow is independent of Poisson's ratio. Figure 5 presents results for the velocity field at a *very low acoustic wave number* ($\gamma = 0.001$) for low and high fluid inertia as a function of Poisson's ratio of the beam material. Note that the velocity field decreases in magnitude as the Poisson ratio increases from $\sigma = 0$ to $\sigma = 0.5$, while its dependence on the coordinate z does not change. Namely, in the low fluid inertia limit, we observe a quasiparabolic flow, while for high fluid inertia, thin boundary layers are present in the immediate vicinity of the channel walls, i.e., at $\bar{z} = \pm 1/2$. These velocity fields exhibit the Poisson ratio rescaling in Eq. (35), which is expected since the flow is essentially incompressible at this very small acoustic wave number (long acoustic wavelength).

In Fig. 6, we present complementary results for a *moderately low acoustic wave number* of $\gamma = 0.1$. Different behavior is observed here, with the effects of fluid compressibility playing a significant role for the low fluid inertia case of $\beta = 0.1$; see Fig. 6(a). This is expected since the fluid compressibility number is $\alpha \equiv \gamma/\beta = 1$, in this case, indicating that compressibility of the fluid is significant. Distortions in the velocity profile in Fig. 6(a) are observed in comparison to Fig. 5(a) (which corresponds to $\alpha = 0.01$). This behavior was discussed in detail in Ref. [21] and is due to nonmonotonic variations in the pressure distribution induced by fluid compressibility effects. Nonetheless, the results in Fig. 6(a) follow the Poisson ratio rescaling in Eq. (35) in agreement with the discussion above (for low fluid inertia, $\beta \ll 10$).

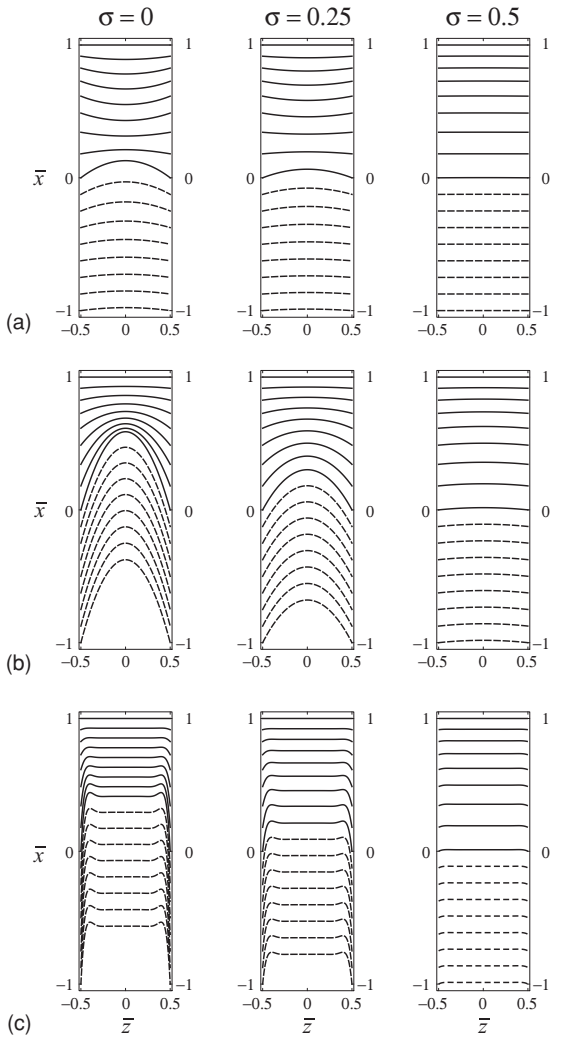

FIG. 6. Velocity profile (magnitude) within the rigid channel-cantilever system showing the effects of Poisson's ratio $\sigma = 0$, 0.25, 0.5 for the *moderately low acoustic wave number* $\gamma = 0.1$. Variation in fluid velocity relative to wall velocity for $\bar{x} \in [-1,\ 1]$ and $\Delta\bar{x} = 0.125$. Note. $\bar{x} = 0$ corresponds to the clamped end of the cantilever. (a) Low fluid inertia, $\beta = 0.1$, (b) moderate fluid inertia, $\beta = 10$, and (c) high fluid inertia, $\beta = 1000$.

As fluid inertia increases, however, we find that while the Poisson ratio rescaling in Eq. (35) captures the dominant behavior, there are some (small) deviations. This is also expected, since for high fluid inertia, Eq. (35) is valid only for a low acoustic wave number, i.e., $\gamma \ll 1$, Figure 6(b) exhibits

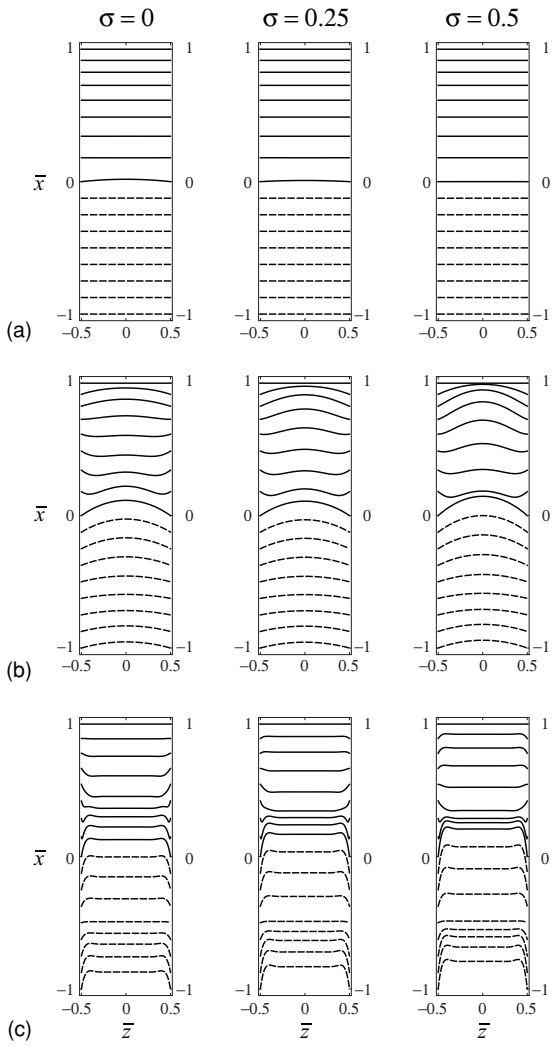

FIG. 7. As for Fig. 6 but for *high acoustic wave number* $\gamma = 10$.

the usual (incompressible) parabolic velocity profile expected for low fluid inertia, since the fluid compressibility number $\alpha = 0.01 \ll 1$ and fluid inertia effects are not strong with $\beta = 10$. Figure 6(c) is indistinguishable from Fig. 5(c) and corresponds to the incompressible high fluid inertia limit.

Figure 7 presents results for the case of a *high acoustic wave number* ($\gamma = 10$), i.e., small acoustic wavelength. Here, acoustic effects in the flow are strong and distort the velocity field significantly from the incompressible flow result. Interestingly, however, the low inertia velocity fields in Fig. 7(a) still satisfy the Poisson ratio rescaling in Eq. (35)—this is in agreement with the above discussion, which predicted that Eq. (35) always holds for low fluid inertia, i.e., $\beta \ll 10$. Since the fluid compressibility number is very large in this case, $\alpha = 100$, compressibility of the fluid strongly distorts the flow, with velocity gradients being concentrated near the clamp; these are just visible in Fig. 7(a).

However, for $\beta = 10$ and $\beta = 1000$ in Figs. 7(b) and 7(c), respectively, the rescaling in Eq. (35) is not exhibited. While the velocity fields show a dependence on Poisson's ratio, the flow magnitude does not decrease with an increasing Poisson ratio. These results are in complete agreement with the discussion above, which predicted that Eq. (35) holds at moderate to high fluid inertia, provided the acoustic wave number is small.

Taken collectively, the results in Figs. 5–7 and the discussion above clearly establish that the Poisson ratio rescaling in Eq. (35) does not hold at moderate to high fluid inertia ($\beta > 10$) with small acoustic wavelength, i.e., $\gamma > 1$. However, since the off-axis flow typically exerts a weak effect on the overall flow (which includes the on-axis flow) in such cases, these results indicate that Eq. (35) accounts for the effects of Poisson's ratio on the total energy dissipation, regardless of fluid inertia. This will be examined in detail below.

2. *Energy dissipation*

In Fig. 8(a), we present results for the scaled energy dissipation (normalized quality factor) of a typical device with an acoustic wave number of $\gamma = 0.03$ [21] and a fixed off-axis channel placement of $\bar{Z}_0 = 0.1$. These results are obtained using the theoretical model in Eqs. (31)–(34) that rigorously accounts for the effects of nonzero Poisson's ratio. Figure 8 clearly demonstrates that increasing Poisson's ratio reduces the effects of off-axis channel placement. This finding is directly in line with the above discussion and is due to a reduction in the volumetric flux induced by the off-axis pumping action—the channel walls contract with axial expansion at nonzero Poisson's ratio; see Eq. (9).

In Fig. 8(b), we present results complementary to Fig. 8(a), whereby the theoretical model is implemented for a Poisson ratio of zero, and the off-axis placement is rescaled in accord with Eq. (35). Comparing Figs. 8(a) and 8(b), it is clear that the rescaling in Eq. (35) of the zero Poisson ratio theory accurately accounts for the Poisson ratio variations.

Importantly, a small discrepancy does exist between Figs. 8(a) and 8(b) for the limiting case of $\sigma = 1/2$, i.e., for an incompressible solid. This effect is accentuated by increasing the off-axis channel placement $\bar{Z}_0$, which also allows the off-axis flow to contribute in the higher inertia regime; see Fig. 9. These results demonstrate that the rescaling in Eq. (35) is valid for all β, provided $\sigma \neq 1/2$; the acoustic wave number is small $\gamma = 0.03 \ll 1$ in line with the above discussion. Even so, Eq. (35) does correctly predict a dramatic reduction in the effects of off-axis channel placement for $\sigma = 1/2$ in comparison to $\sigma = 0$, as observed in Figs. 8(a) and 9(a).

In Fig. 9, there is a clear deviation between the rescaling of the zero Poisson ratio solution and the exact result for $\sigma = 1/2$. Equation (35) erroneously predicts that off-axis placement has no effect in this limiting case. This deviation is expected since Eq. (35) simply accounts for the net volume change in the channel, while ignoring the additional mechanism due to finite fluid compressibility. This latter effect results in pumping of fluid into and out of the channel, despite a zero net volume change in the channel at $\sigma = 1/2$, as we will now investigate.

3. *Volumetric flux*

To illustrate this fluid compressibility effect at Poisson's ratio of $\sigma = 1/2$, we present results for the volumetric flux at the inlet of the rigid channel as a function of Poisson's ratio in Fig. 10. This is calculated for fixed β as the normalized wave number γ is varied. Note that, for small

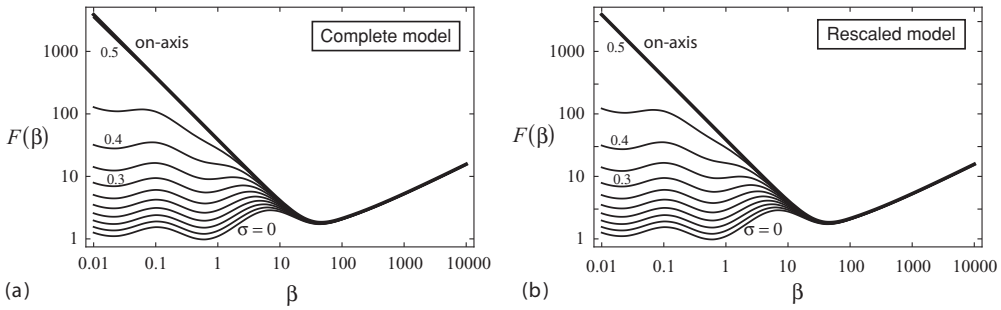

FIG. 8. Plot of normalized quality factor $F(\beta)$ vs β as a function of (a) Poisson's ratio varying in range from $0 \leqslant \sigma \leqslant 0.5$ in increments of 0.05, for a fixed off-axis placement of $\bar{Z}_0 = 0.1$, normalized lead channel length of $\bar{L}_c = 1$, and normalized acoustic wave number of $\gamma = 0.03$ and (b) Poisson's ratio of $\sigma = 0$ in the theoretical model and a rescaled off-axis placement according to Eq. (35). The on-axis solution ($\bar{Z}_0 = 0$) is shown for reference (heavy curve). For the parameters shown, comparison between (a) and (b) reveals that the rescaled model accurately accounts for the effect of nonzero Poisson ratio ($\sigma < 0.5$).

normalized wave number γ, the volumetric flux decreases with increasing Poisson's ratio. This is expected, since the flow is approximately incompressible in this limit, and increasing Poisson's ratio reduces the net volume change in the channel. However, above a normalized wave number of order unity, varying the Poisson ratio has little effect on the volumetric flux into the channel. This is precisely the regime where acoustic (compressibility) effects in the fluid are dominant, leading to acoustic resonances in the channel. While there is some variation in the peak volumetric flux at these resonances, this variation is weak in comparison to the incompressible fluid solution ($\gamma \to 0$) for $\sigma = 1/2$ that yields zero volumetric flux. Positions of the acoustic resonances are unaffected by Poisson's ratio, as expected.

4. Fluid pressure

Next, we examine the effects of Poisson's ratio on the maximum pressure induced by the off-axis flow, results for which are given in Fig. 11. A detailed discussion of the zero Poisson ratio results of Fig. 11(a) were presented in Ref. [21], and, thus, we focus on the effects of Poisson's ratio only. Figure 11 clearly demonstrates that increasing Poisson's ratio reduces the maximum pressure in the channel, with the effect being more pronounced at low β, i.e., low inertia. Mechanisms leading to this behavior are now studied.

In the low inertia limit, the viscous boundary layers generated at the channel walls strongly overlap, and extension and compression of the channel lead to significant dilation of the fluid by the pumping mechanism. Increasing Poisson's ratio reduces this dilational effect because the net volume change in the channel decreases with increasing Poisson's ratio. In contrast, at high β, the viscous boundary layers are tightly confined to the channel walls, leading to (approximate) plug flow outside the boundary layers. Thus, the pressure distribution in the high inertia regime is dominated by acceleration of this plug flow as the channel moves.

To fully explore this feature at high β (which corresponds to incompressible fluid flow), we examine the functional form of the pressure gradient. From Eqs. (20b), (20e), and (24), we obtain the following result in the incompressible fluid limit ($\alpha \to 0$):

$$\frac{d\bar{P}}{d\bar{x}} = (1-2\sigma)(B - i\beta)\,S(\bar{x}) + i\beta[1 + S(\bar{x})]. \qquad (37)$$

For high β, $|B| \ll \beta$ as illustrated in Fig. 4, and, thus, Eq. (37) reduces to

$$\frac{d\bar{P}}{d\bar{x}} \approx -i\beta\,[(1-2\sigma)S(\bar{x}) - 1 - S(\bar{x})], \quad \beta \gg 1. \qquad (38)$$

Equation (38) clearly establishes that the scaling in Eq. (35) does not apply to the pressure in the incompressible fluid limit. This is because acceleration of the fluid is always present in the plug flow region, regardless of the Poisson ratio. This acceleration is the mechanism that gives rise to the pressure distribution of Eq. (38). As such, Poisson's ratio exerts a relatively weak effect in this high inertia regime as observed in Fig. 11.

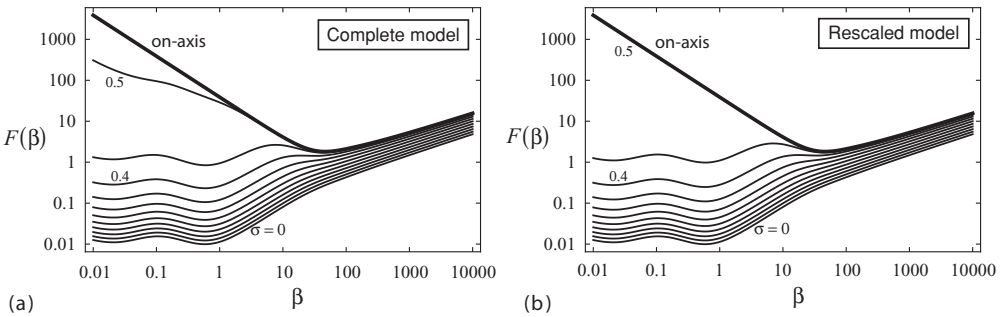

FIG. 9. As for Fig. 8, with fixed off-axis placement of $\bar{Z}_0 = 1$.

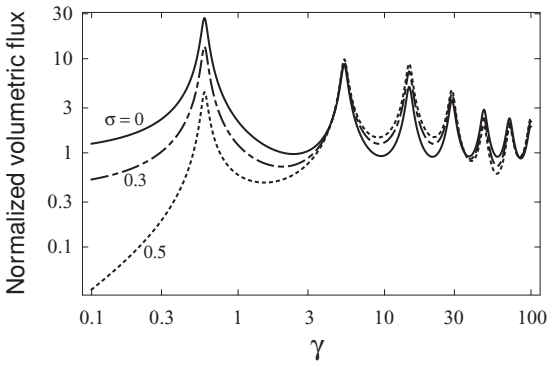

FIG. 10. Plot of normalized volumetric flux into the inlet of the rigid channel, for $\beta = 1000$, as a function of normalized wave number γ and Poisson's ratio σ. Volumetric flux scale is $q_s = u_s h_{\text{fluid}} b_{\text{fluid}}$.

In the opposite limit of low inertia (low β), the viscous boundary layers strongly overlap, and fluid compressibility effects are dominant; note that $\alpha = \gamma/\beta$. Consequently, the pressure distribution is generated primarily by shearing and compression of the fluid as the channel contracts and expands. In this regime, $|B| \gg \beta$ and the governing equation for the associated pressure function $h(X)$ becomes

$$\frac{d^2h}{d\bar{x}^2} + i\alpha B\, h \approx i\alpha B(1-2\sigma)S(\bar{x}), \tag{39}$$

provided $\sigma \neq 1/2$. Since the right hand side of Eq. (39) is directly proportional to $1-2\sigma$, it immediately follows that the rescaling in Eq. (35) holds true. The pressure distribution induced by acceleration of the fluid is comparatively small in this case, which is dominated by viscous and compressibility effects. This fluid acceleration (inertia) effect only presents itself in the singular limit $\sigma = 1/2$.

Therefore, we conclude that Poisson's ratio dependencies of the pressure distribution differ greatly in the low and high inertia regimes as observed in Fig. 11.

D. Comparison to experimental measurements

In this section, we present a comparison of the arbitrary Poisson ratio theory in Eqs. (31)–(34) to detailed experimental measurements. These measurements were reported in our previous paper that investigated the effects of higher order modes [22]. They were performed using a glycerol-water mixture, allowing for the viscosity to be varied over 3 orders of magnitude. The geometric and mechanical properties of these (silicon) cantilevers are given in Table I. These devices have different channel thicknesses, ensuring measurements span the low to high inertia flow regimes. The reader is referred to Ref. [22] for details of the measurements and these devices. The Poisson ratio of these devices is taken to be $\sigma = 0.25$ [27] in the analysis below.

The only unknown parameter in the model is the off-axis placement of the channel $\bar{Z}_0$. Since $\bar{Z}_0$ is a fixed geometric property of each device, its value cannot vary between mode number. As such, $\bar{Z}_0$ was obtained by only fitting results for the fundamental mode of each device; theoretical results for mode 2 were then calculated using this fixed value. This provides a consistency check and assessment on the validity of the theoretical model. This fitting procedure involved adjusting $\bar{Z}_0$ to minimize the difference between the theoretical model in Eqs. (31)–(34) and the measured normalized quality factors for the fundamental mode (mode 1) over the entire viscosity

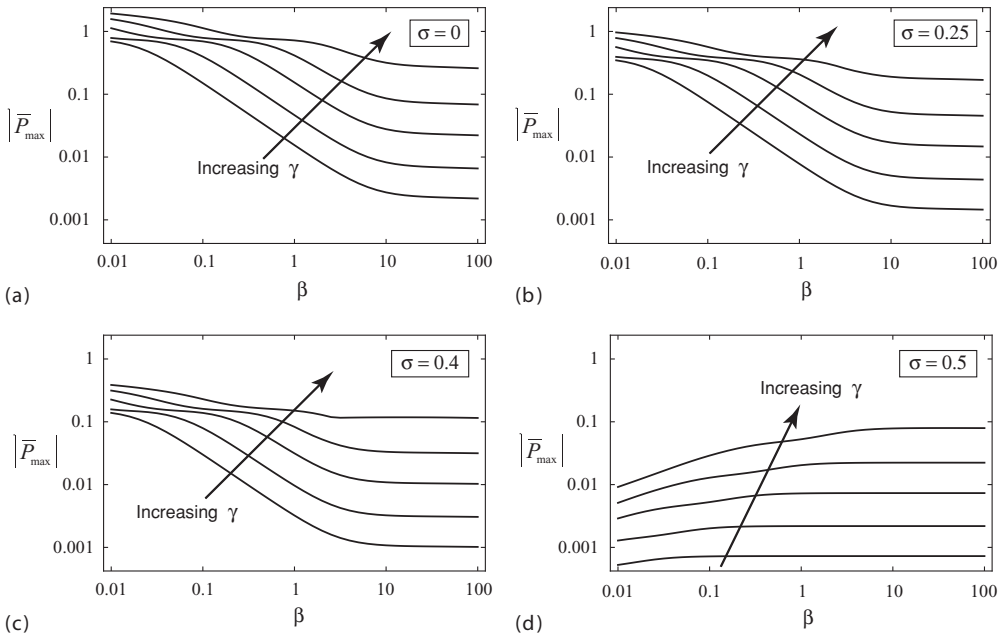

FIG. 11. Magnitude of normalized maximum pressure $|\bar{P}_{\max}|$ within the rigid channel-cantilever system for various normalized acoustic numbers $\gamma = 0.001, 0.003, 0.01, 0.03, 0.1$ and Poisson's ratios: (a) $\sigma = 0$, (b) $\sigma = 0.25$, (c) $\sigma = 0.4$, and (d) $\sigma = 0.5$. The pressure scale is $P_s = \rho_0 c^2 u_s/(\omega L)$ and is appropriate for the low inertia compressible limit, i.e., $\beta \ll 1$ and $\alpha \gg 1$ [21]. The length of the rigid lead channel equals the cantilever length, i.e., $L_c = L$. Identical axis scales have been used in each figure to assist comparison.

TABLE I. Dimensions and beam resonance properties for three devices used in comparison. Resonant frequencies are given for air. The specified fluid channel width of the theoretical model b_{fluid} is the sum of the two parallel channel widths in the actual devices as required in the theoretical model.

							Resonances			
	Dimensions (μm)						Mode 1		Mode 2	
Device	h_{fluid}	b_{fluid}	h_{cant}	b_{cant}	L	L_c	f_1^{res} (kHz)	Q_1^{air}	f_2^{res} (kHz)	Q_2^{air}
A	3	16	7	33	210	207.5	218.9	17919	1354.1	7092
B	8	16	12	33	210	207.5	411.6	8583	2476.0	4739
C	15	40	19	57	321	240	275.1	4068	1663.9	5093

range considered. Independent measurement of $\bar{Z}_0$ was not possible in the current experimental setup.

Good agreement between theory and measurement was observed in Ref. [22], which implicitly assumed a Poisson ratio of zero. The above theoretical discussion establishes that Poisson's ratio has the effect of rescaling the off-axis placement; see Eq. (35). Therefore, we expect to see similar agreement with the full nonzero Poisson ratio theory of Eqs. (31)–(34), provided the off-axis placement in the zero Poisson ratio theory of Refs. [20–22] is rescaled in accord with Eq. (35).

Figure 12 gives a comparison of the measured normalized quality factor with the theoretical model presented in Eqs. (31)–(34) for the fundamental mode of vibration (mode 1). The off-axis channel placement $\bar{Z}_0$ was used as a fitting parameter in this comparison. As predicted above, the fitted values of $\bar{Z}_0$ are a factor $\approx 1/(1-2\sigma) = 2$ higher than those obtained in Ref. [22] (which used zero Poisson's ratio). By comparing Fig. 12 with Fig. 11 of Ref. [22], we find that the theoretical predictions using the nonzero Poisson ratio are almost identical to the zero Poisson ratio theory under the rescaling in Eq. (35). We emphasize that the terms compressible and incompressible in Figs. 12 and 13 refer to the fluid only—the solid is always compressible in these devices as dictated by the Poisson ratio.

Complementary results for mode 2 are given in Fig. 13 and are virtually identical to Fig. 12 of Ref. [22]. We again emphasize that the off-axis placements $\bar{Z}_0$ were taken from fits to the fundamental mode in Fig. 12. This provides strong evidence for the robustness of the model.

These results serve to demonstrate (i) the validity of the full model in Eqs. (31)–(34) that rigorously includes the effects of the nonzero Poisson ratio and (ii) rescaling of the zero Poisson theory presented in Eq. (35).

While these results illustrate the validity of the model, they also highlight differences between the model and the

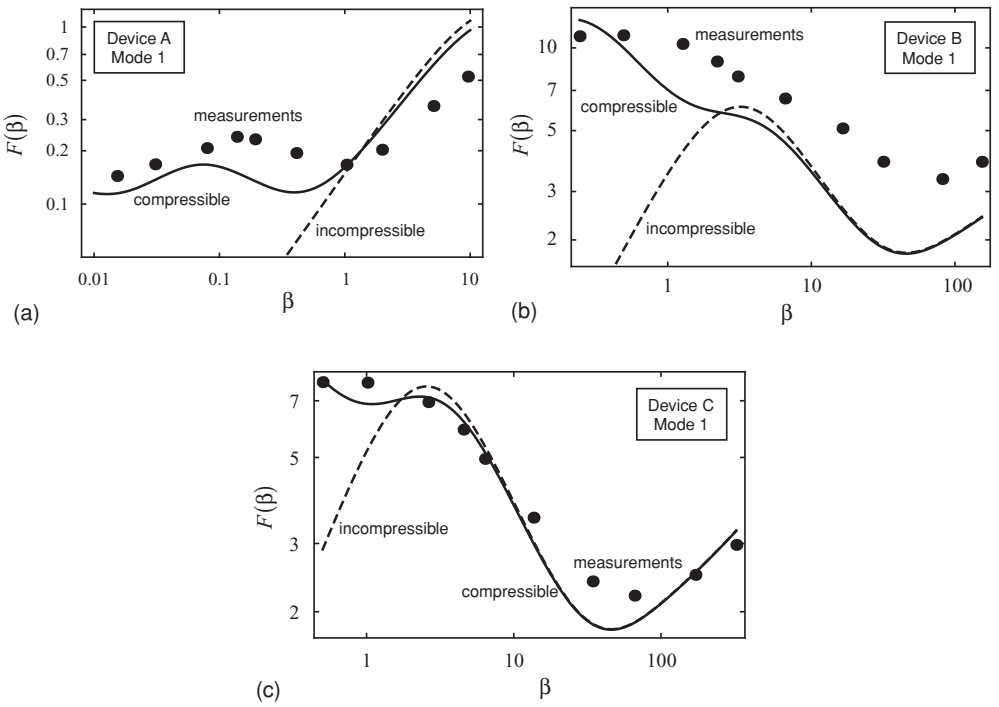

FIG. 12. Fundamental mode (mode 1). Comparison of theoretical model (lines) to measurements (solid circles) for devices A, B, and C. The off-axis placement for each device: A ($\bar{Z}_0 = 0.5$); B ($\bar{Z}_0 = 0.1$); C ($\bar{Z}_0 = 0.09$). Solid line (compressible fluid—finite speed of sound). Dashed line (incompressible fluid—infinite speed of sound).

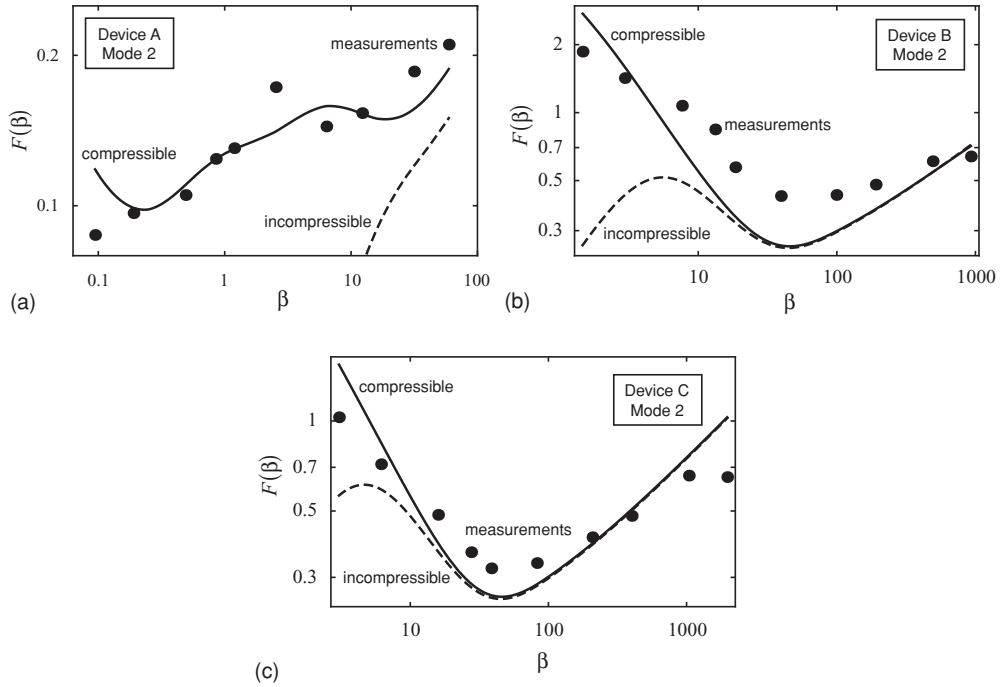

FIG. 13. Second mode (mode 2). Comparison of theoretical model (lines) to measurements (solid circles) for devices A, B, and C. The off-axis placement for each device: A ($\bar{Z}_0 = 0.5$); B ($\bar{Z}_0 = 0.1$); C ($\bar{Z}_0 = 0.09$). Solid line (compressible fluid–finite speed of sound). Dashed line (incompressible fluid–infinite speed of sound).

measurements on practical devices. These differences are not unexpected, given the level of approximation in the model. Most importantly, the model implicitly assumes (i) a cantilever beam whose length greatly exceeds its width and thickness, and (ii) the fluid channel width is much larger than its thickness; see the assumptions in Sec. II. Examination of the device dimensions in Table I reveals that these assumptions may not strictly hold for the devices investigated. Nonetheless, the agreement between the model and the measurements is good and indicates that the level of approximation is appropriate for extracting the central effects. For a more complete discussion of these approximations and suggestions for their improvement, the reader is referred to Secs. 3.4 and 3.5 of Ref. [21].

E. Practical recommendations

The above results and analysis demonstrate that the dominant effect of Poisson's ratio on the quality factor is to simply rescale the off-axis channel placement, resulting in an effective off-axis channel placement

$$Z_{\text{eff}} \approx (1 - 2\sigma)\, Z_{\text{off-axis}}. \tag{40}$$

The question may then be asked as to which model should be implemented in practice: (i) the (arbitrary Poisson ratio) model presented here in Eqs. (31)–(34) or (ii) the original (zero Poisson ratio) model combined with the rescaling in Eq. (40). Since both models exhibit similar complexity and accuracy, it is recommended that the model with the arbitrary Poisson ratio be used in practice. This will inherently avoid any omissions due to the finite Poisson ratio, which are not captured by Eq. (40). Such situations include (i) the rare case where an incompressible solid ($\sigma = 1/2$) is studied, (ii) the effect of acoustic-resonance effects in the flow at high fluid inertia (see Fig. 10), and (iii) the effect of Poisson's ratio on the pressure distribution in the channel also at high inertia flows (see Fig. 11). Importantly, truly incompressible solids are rarely encountered, acoustic resonances are difficult to realize, as discussed in Ref. [22], and the off-axis flow at high inertia has little effect on the quality factor except in the presence of acoustic resonances [22]. Therefore, these considerations do not affect the device quality factor in most cases of practical interest.

Nonetheless, Eq. (40) provides important information that can be used in engineering and design to gain an initial understanding of the effects of Poisson's ratio and to modify the energy dissipation of microfluidic beam resonators. Since decreasing Z_{eff} reduces the effects of any off-axis flow, the use of materials with high Poisson's ratio σ is very desirable. This can potentially improve the sensitivity of frequency shift (mass) measurements, which is one of the primary applications of these devices.

IV. CONCLUSIONS

We have investigated the effect of Poisson's ratio on energy dissipation in microfluidic beam resonators. This included a rigorous derivation of the displacement field of the Euler-Bernoulli beam theory and a commensurate treatment of the fluid-structure interaction problem. It was found that Poisson's ratio had no effect on energy dissipation provided the fluid channel was placed precisely on the neutral axis of the beam. In contrast, off-axis placement generates an additional flow that is strongly dependent on Poisson's ratio.

For many cases of practical interest, it was shown that off-axis channel placement and Poisson's ratio (approximately) appear as a single term $(1-2\sigma)\,z_0$ in the model. This establishes that (i) rescaling $z_0 \to (1-2\sigma)\,z_0$ accounts for the dominant effects of Poisson's ratio, and (ii) the use of a high Poisson ratio beam material can reduce the effects of off-axis placement and, thus, enhance the quality factor. The validity of this Poisson ratio effect also was demonstrated by comparison to detailed measurements on a series of devices that span the low to high inertia regimes. These results are expected to be of significant practical value, allowing for greater flexibility in the design and application of microfluidic beam resonators.

ACKNOWLEDGMENTS

This work was supported by the Institute of Collaborative Biotechnologies through Contract No. W911NF-09-D-0001 from the US Army Research Office and the NIH Cell Decision Process Center Grant No. P50-GM68762. T.P.B. acknowledges support by the Max Planck Society and the MPI for Biophysical Chemistry. J.L. acknowledges support from the Sogang University (Grant No. 201010087.01). J.E.S. acknowledges support from the Australian Research Council grants scheme.

APPENDIX: DISPLACEMENT FIELD OF EULER-BERNOULLI BEAM THEORY

In this Appendix, we present a derivation of the displacement field of the Euler-Bernoulli beam theory from first principles [23,24] while emphasizing the key underlying assumptions of this classical theory. This provides the motivation and foundation for the fluid-structure interaction model developed in this paper.

Consider a long slender elastic beam whose major axis is oriented in the x direction as in Fig. 2. The beam surface is unrestrained, i.e.,

$$\mathbf{n}\cdot\mathbf{T}\,|_{\text{surface}} = \mathbf{0}, \tag{A1}$$

where $\mathbf{n}$ is the unit normal to the beam surface and $\mathbf{T}$ is the stress tensor. Since (i) the beam length (along the x direction) greatly exceeds its cross-sectional dimensions (in the y and z directions), and (ii) the corresponding normal components of the stress tensor are zero at the surface [Eq. (A1)], it then follows that all components in Eq. (A1) are zero throughout the beam cross section, to leading order, i.e.,

$$\mathbf{n}\cdot\mathbf{T}|_{\text{for all } x,\,y,\,z} = \mathbf{0}. \tag{A2}$$

Note that this approximation is correct to linear order in the y and z coordinates, and higher order (quadratic) corrections are ignored. Within this approximation, Eq. (A2) establishes that all stress components T_{ij} are zero, apart from the normal stress T_{xx} whose dependence on x depends on specifics of the beam and load.

Next, we consider Hooke's law for an isotropic solid,

$$\mathbf{T} = \frac{E}{1+\sigma}\left(\mathbf{e} + \frac{\sigma}{1-2\sigma}\operatorname{tr}\mathbf{e}\,\mathbf{I}\right), \tag{A3}$$

where $\mathbf{e}$ is the strain tensor, $\mathbf{I}$ is the identity tensor, E is the Young's modulus, and σ is the Poisson ratio. From Eqs. (A2) and (A3), it then follows that the corresponding nonzero stress and strain components can only be specified to linear order in the y and z coordinates. This provides a fundamental restriction on the analysis.

To proceed, we then express the strain tensor $\mathbf{e}$ in terms of the beam displacement field

$$\mathbf{u} = u\,\hat{\mathbf{x}} + v\,\hat{\mathbf{y}} + w\,\hat{\mathbf{z}}, \tag{A4}$$

while noting that the only nonzero stress component is T_{xx}. Equation (A3) then yields the following constraints on the displacement:

$$\frac{\partial v}{\partial x} = -\frac{\partial u}{\partial y}, \quad \frac{\partial w}{\partial x} = -\frac{\partial u}{\partial z}, \quad \frac{\partial w}{\partial y} = -\frac{\partial v}{\partial z}, \tag{A5a}$$

$$\frac{\partial w}{\partial z} = -\frac{\sigma}{1-\sigma}\left(\frac{\partial u}{\partial x}+\frac{\partial v}{\partial y}\right), \quad \frac{\partial v}{\partial y} = -\frac{\sigma}{1-\sigma}\left(\frac{\partial u}{\partial x}+\frac{\partial w}{\partial z}\right) \tag{A5b}$$

We consider a beam whose cross section is symmetric about $y=0$ and $z=0$, which is relevant to the microfluidic beam resonator considered here, while noting that the analysis can easily be generalized [23,24].

Since the stress and strain are specified to linear order in the cross-sectional coordinates y and z, we formally expand all displacement components in a double power series in y and z

$$\begin{aligned} u(x,y,z) &= \sum_{m=0}^{\infty}\sum_{n=0}^{\infty} u_{mn}(x)\,y^m z^n, \\ v(x,y,z) &= \sum_{m=0}^{\infty}\sum_{n=0}^{\infty} v_{mn}(x)\,y^m z^n, \\ w(x,y,z) &= \sum_{m=0}^{\infty}\sum_{n=0}^{\infty} w_{mn}(x)\,y^m z^n, \end{aligned} \tag{A6}$$

where the functions $u_{mn}(x)$, $v_{mn}(x)$, and $w_{mn}(x)$ are to be determined.

It is assumed that the net force along the major axis of the beam is zero, and thus, stretching of the beam in the x direction is zero, i.e., $u_{00}(x)=0$. We consider deflections in the z direction only and no torsion, i.e., $v_{00}(x)=0$ and $w_{10}(x)=0$, respectively. Substituting Eq. (A6) into Eq. (A5) and equating powers up to linear order y and z, yields the following solution:

$$\begin{aligned} &u_{01}(x) = -\frac{dw_{00}}{dx}, \quad u_{10}(x)=u_{11}(x)=u_{02}(x)=u_{20}(x)=0, \\ &v_{11}(x) = \sigma\frac{d^2w_{00}}{dx^2}, \quad v_{10}(x)=v_{02}(x)=v_{20}(x)=0, \\ &w_{02}(x) = -w_{20}(x) = \frac{\sigma}{2}\frac{d^2w_{00}}{dx^2}, \\ &w_{01}(x) = w_{10}(x) = w_{11}(x) = 0. \end{aligned} \tag{A7}$$

Note that displacement components up to and including quadratic order in y and z are required to ensure strain components are specified to be correct to linear order. Substituting Eq. (A7) into Eq. (A6) then gives the required expression

for the displacement field that is consistent with the specified stress distribution,

$$u(x,y,z) = -z\frac{dw_{00}}{dx}, \tag{A8a}$$

$$v(x,y,z) = \sigma yz\frac{d^2w_{00}}{dx^2}, \tag{A8b}$$

$$w(x,y,z) = w_{00}(x) + \frac{\sigma}{2}(z^2 - y^2)\frac{d^2w_{00}}{dx^2}. \tag{A8c}$$

This result rigorously accounts for distortion of the beam cross section due to the effect of Poisson's ratio; see Fig. 3. Substitution of Eq. (A8) into Eq. (A3) then yields the stress tensor,

$$\mathbf{T} = -Ez\frac{d^2w_{00}}{dx^2}\hat{\mathbf{x}}\hat{\mathbf{x}}, \tag{A9}$$

which is the well-known result for pure bending of a beam [23,24]. Equation (A8) is used in Sec. II to calculate the flow generated in the channel under the replacement $W \equiv w_{00}$.

[1] N. V. Lavrik, M. J. Sepaniak, and P. G. Datskos, Rev. Sci. Instrum. **75**, 2229 (2004).

[2] K. L. Ekinci and M. L. Roukes, Rev. Sci. Instrum. **76**, 061101 (2005).

[3] M. E. Motamedi, *Method of Fabricating a Cantilever Beam for a Monolithic Accelerometer* (US Patent Number 4,670,092, 1987).

[4] F. J. Giessibl, Rev. Mod. Phys. **75**, 949 (2003).

[5] H.-J. Butt, P. Siedle, K. Seifert, K. Fendler, T. Seeger, E. Bamberg, A. L. Weisenhorn, K. Goldie, and A. Engel, J. Microsc. **169**, 75 (1993).

[6] J. E. Sader, J. Appl. Phys. **84**, 64 (1998).

[7] J. W. M. Chon, P. Mulvaney, and J. E. Sader, J. Appl. Phys. **87**, 3978 (2000).

[8] T. Naik, E. K. Longmire, and S. C. Mantell, Sens. Actuators, A **102**, 240 (2003).

[9] M. R. Paul and M. C. Cross, Phys. Rev. Lett. **92**, 235501 (2004).

[10] T. Braun, V. Barwich, M. K. Ghatkesar, A. H. Bredekamp, Ch. Gerber, M. Hegner, and H. P. Lang, Phys. Rev. E **72**, 031907 (2005).

[11] R. J. Clarke, S. M. Cox, P. M. Williams, and O. E. Jensen, J. Fluid Mech. **545**, 397 (2005).

[12] S. Basak, A. Raman, and S. V. Garimella, J. Appl. Phys. **99**, 114906 (2006).

[13] C. A. Van Eysden and J. E. Sader, J. Appl. Phys. **101**, 044908 (2007).

[14] C. A. Van Eysden and J. E. Sader, J. Appl. Phys. **106**, 094904 (2009).

[15] C. Castille, I. Dufour, and C. Lucat, Appl. Phys. Lett. **96**, 154102 (2010).

[16] J. L. Arlett and M. L. Roukes, J. Appl. Phys. **108**, 084701 (2010).

[17] T. P. Burg, M. Godin, S. M. Knudsen, W. Shen, G. Carlson, J. S. Foster, K. Babcock, and S. R. Manalis, Nature (London) **446**, 1066 (2007).

[18] J. Lee, W. Shen, K. Payer, T. P. Burg, and S. R. Manalis, Nano Lett. **10**, 2537 (2010).

[19] J. Lee, A. K. Bryan, and S. R. Manalis, Rev. Sci. Instrum. **82**, 023704 (2011).

[20] T. P. Burg, J. E. Sader, and S. R. Manalis, Phys. Rev. Lett. **102**, 228103 (2009).

[21] J. E. Sader, T. P. Burg, and S. R. Manalis, J. Fluid. Mech. **650**, 215 (2010).

[22] J. E. Sader, J. Lee, and S. R. Manalis, J. Appl. Phys. **108**, 114507 (2010).

[23] S. Timoshenko and D. H. Young, *Elements of Strength of Materials* (D. Van Nostrand Company, New York, 1968).

[24] L. D. Landau and E. M. Lifshitz, *Theory of Elasticity*, 2nd ed. (Pergamon Press, Oxford, 1970).

[25] G. K. Batchelor, *An Introduction to Fluid Dynamics* (Cambridge University Press, Cambridge, UK, 1974).

[26] This parameter is often referred to under different names, e.g., Reynolds, inverse Stokes, or Womersley number.

[27] J. J. Wortman and R. A. Evans, J. Appl. Phys. **36**, 153 (1965). The long axis of the silicon cantilevers is oriented in the [110] direction. The Poisson ratios in the corresponding two orthogonal directions [1$\bar{1}$0] and [001] are 0.07 and 0.36, respectively. A value of $\sigma = 0.25$ is chosen in the (isotropic) theoretical model to approximate the net volume change in the crystalline solid.